PAPER

Compositions and thermoelectric properties of XNiSn (X = Ti, Zr, Hf) half-Heusler alloys

R. A. Downie,[a] S. A. Barczak,[a] R. I. Smith[b] and J. W. G. Bos*[a]

Rietveld analysis of neutron powder diffraction data has been used to investigate the compositions of XNiSn (X = Ti, Zr, Hf) half-Heusler alloys prepared by solid state reactions. All samples containing Ti have 2–3% excess Ni, whereas the samples with X = Zr, Hf are almost stoichiometric. Samples with mixed X-metals are characterised by the presence of 3–4 distinct $X_{1-x}X'_xNi_{1+y}Sn$ half-Heusler phases. Variable temperature and time dependent neutron powder diffraction for X = Ti and X = $Ti_{0.5}Hf_{0.5}$ demonstrates that both the amount of excess Ni and the phase distribution are stable up to at least 600 °C. Debye temperatures of 367(2) K and 317(2) K were obtained from the thermal displacement parameters. The samples containing Ti are characterised by a ~0.15 eV bandgap and a monotonously decreasing Seebeck coefficient. The compositions with Zr and Hf have similar bandgap values but show ambipolar transitions. Analysis of the thermoelectric transport data of degenerately doped $Ti_{0.5}Zr_{0.5}NiSn_{1-z}Sb_z$ samples using a single parabolic band model demonstrates that the transport is limited by alloy scattering and yielded an effective carrier mass of 2.5(1) m_e.

Introduction

Half-Heuslers (HHs) show great promise in the field of thermo-electric waste heat recovery, in which they can be used to improve the energy efficiency of any heat-generating process.[1] The performance of a thermoelectric material is determined by its figure of merit, $zT = S^2T/\rho\kappa$, where S is the Seebeck coefficient, ρ is the electrical resistivity, κ is the sum of the lattice (κ_{lat}) and electronic (κ_{el}) thermal conductivities, and T is the absolute temperature. The large power factors (S^2/ρ) possessed by HHs make them an obvious choice for thermoelectrics research, but high κ values mean that alterations to the structure must be made to reduce κ_{lat} and achieve high zT values.[2–6]

Recently, phases on the XNiSn–XNi$_2$Sn HH full-Heusler (FH) pseudo-binary have generated substantial interest (where X = Ti, Zr, Hf).[3,5,6] The addition of excess Ni has been found to have a significant impact on the thermoelectric properties. In particular, large reductions in the thermal conductivity of TiNi$_{1+y}$Sn samples have been reported.[7–13] In addition, simultaneously enhanced S and electrical conductivity ($\sigma = 1/\rho$) was reported for Zr$_{0.25}$Hf$_{0.75}$Ni$_{1+y}$Sn,[14] and enhanced S with only a minor reduction in σ has been found in Ti$_{0.1}$Zr$_{0.9}$Ni$_{1+y}$Sn and p-type Ti$_{0.5}$Hf$_{0.5}$Co$_{1+y}$Sn$_{0.9}$Sn$_{0.1}$.[15,16] Simultaneous improvements in S

and σ are not expected in homogenous semiconductors, where they depend inversely on carrier concentration.[1] The observation of this effect therefore suggests that potential barriers, due to FH nano-inclusions, filter out low energy carriers leading to an enhancement of S.[17] Indeed, the formation of FH nano-inclusions within the HH matrix has been reported in many of these studies.[8–10,13–16] However, not all samples containing excess Ni ($y > 0$) show enhancements of S and σ, and other reports observe only micro-inclusions of the FH phase.[11,12] We recently reported an in-depth study of TiNiM$_y$Sn (M = Co, Ni, and Cu) nanocomposites prepared via solid state reactions and showed that the excess metal is relatively homogeneously distributed with an upper limit <2 nm for any segregated TiNi$_2$Sn FH inclusions.[18] The absence of clear inclusions demonstrates that the degree of segregation is sensitively dependent on the sample processing, which is in keeping with the wide variety of nanostructures reported in the literature.[3,6] Another topical issue in this field regards the low κ (=2–3 W m^{-1} K^{-1}) that is sometimes observed in XNiSn and XCoSb samples with mixtures of Ti, Zr and Hf, and which is important to underpin $ZT > 1$.[19–23] Recent studies have linked the low κ to phase segregation into multiple half-Heusler phases with different ratios of X-metals.[6,21,24] However, our results for the Ti$_{1-x}$Zr$_x$NiSn series indicate that this multiphase behaviour is kinetically con-trolled, and has a secondary impact on $\kappa(T)$ after alloy scattering, suggesting that the presence of all three of Ti, Zr and Hf is needed.[25] Other approaches aimed at minimising κ_{lat} include off-stoichiometric X$_9$Ni$_7$Sn$_8$ (X = Ti, Zr) compositions that form a HH matrix and a number of segregated phases,[26,27] addition

a Institute of Chemical Sciences and Centre for Advanced Energy Storage and Recovery, School of Engineering and Physical Sciences, Heriot-Watt University, Edinburgh, EH14 4AS, UK. E-mail: j.w.g.bos@hw.ac.uk

b ISIS Facility, Rutherford Appleton Laboratory, Harwell Oxford, Didcot, OX11 0QX, UK

of a $Ti_{70.5}Fe_{29.5}$ eutectic,[28] InSb inclusions in $TiCoSb$,[29,30] and phase segregation involving mixtures of HH phases.[31]

Neutron powder diffraction is a powerful tool to characterise metal-rich HH alloys due to the excellent scattering contrast between the elements present.[7,18,32] In addition, the bulk nature of the technique means a representative average picture is obtained. For the $TiNiM_ySn$ (M = Co, Ni, and Cu) nanocomposites it was possible to account for all excess metal present in the sample.[18] In case of the M = Ni series, the excess Ni was divided over the matrix (nano-inclusions with diameter < 2 nm) and over a distinct FH phase with the sum of excess Ni equal to the nominal y value. This analysis also allowed us to determine that Co substitutes in the matrix, while Cu is part of a nanosegregated FH phase. Here we have extended this approach to the high-zT $XNiSn$ and $X_{0.5}X'_{0.5}NiSn$ parent materials. This has enabled the accurate determination of the experimental compositions, and of the multiphase behaviour that occurs in these samples. In addition, we also present a detailed thermoelectric property analysis of degenerately and non-degenerately doped $XNiSn$ and $X_{0.5}X'_{0.5}NiSn$ compositions.

Experimental

The synthesis of the $XNiSn$ and $X_{0.5}X'_{0.5}NiSn$ (X, X' = Ti, Zr or Hf) samples has been reported in ref. 25. Neutron powder diffraction data for these samples were collected on the upgraded POLARIS instrument at the ISIS facility, Rutherford Appleton Laboratory, UK. Powders were loaded into cylindrical sample cans and diffraction data were collected at room temperature for 300 μA h proton beam current to the ISIS target, corresponding to ~2 hours neutron beam time. In addition, two samples were studied at elevated temperatures: $TiNiSn$ (373 to 973 K in 100 K steps) and $Ti_{0.5}Hf_{0.5}NiSn$ (293, 473, 673 and 873 K). The neutron scattering lengths are b_{Ti} = −3.4 fm, b_{Zr} = 7.2 fm, b_{Hf} = 7.7 fm, b_{Ni} = 10.3 fm and b_{Sn} = 6.2 fm. Crystal structure refinement was by the Rietveld method using the GSAS suite of programs and the EXPGUI graphical interface.[33,34] Profile function three for time-of-flight data in GSAS was used to fit the peak shape. The thermoelectric characterisation for these samples was reported in ref. 25 but no data fitting was undertaken in that study.

Results

1. Room temperature structures

A convenient way to view the $XNiSn$ half-Heusler structure is as a face-centred-cubic lattice of Sn, where all the octahedral holes are occupied by X and half the tetrahedral holes (herein Y1) are filled with Ni. This leaves half the tetrahedral holes empty (Y2). The Y2 sites are fully occupied in the Heusler structure, leading to an increase in space group symmetry (from $F\bar{4}3m$ to $Fm\bar{3}m$) and lattice parameter ($\Delta a \sim 0.2$ Å). $TiNiSn$ is semiconducting with strong hybridisation between Ni and Sn s- and p-orbitals, while the valence and conduction bands are formed by hybridisation of the Ti and Ni d-orbitals.[35] $TiNi_2Sn$ in contrast is

metallic,[35] and this difference in chemical bonding is responsible for the absence of solid solution formation.[36–42]

$TiNiSn$, $ZrNiSn$ and $HfNiSn$. The Rietveld fits to the POLARIS data are presented in Fig. 1. A single half-Heusler phase was used in the fits and the resulting lattice and atomic parameters are reported in Table 1. These agree well with previously
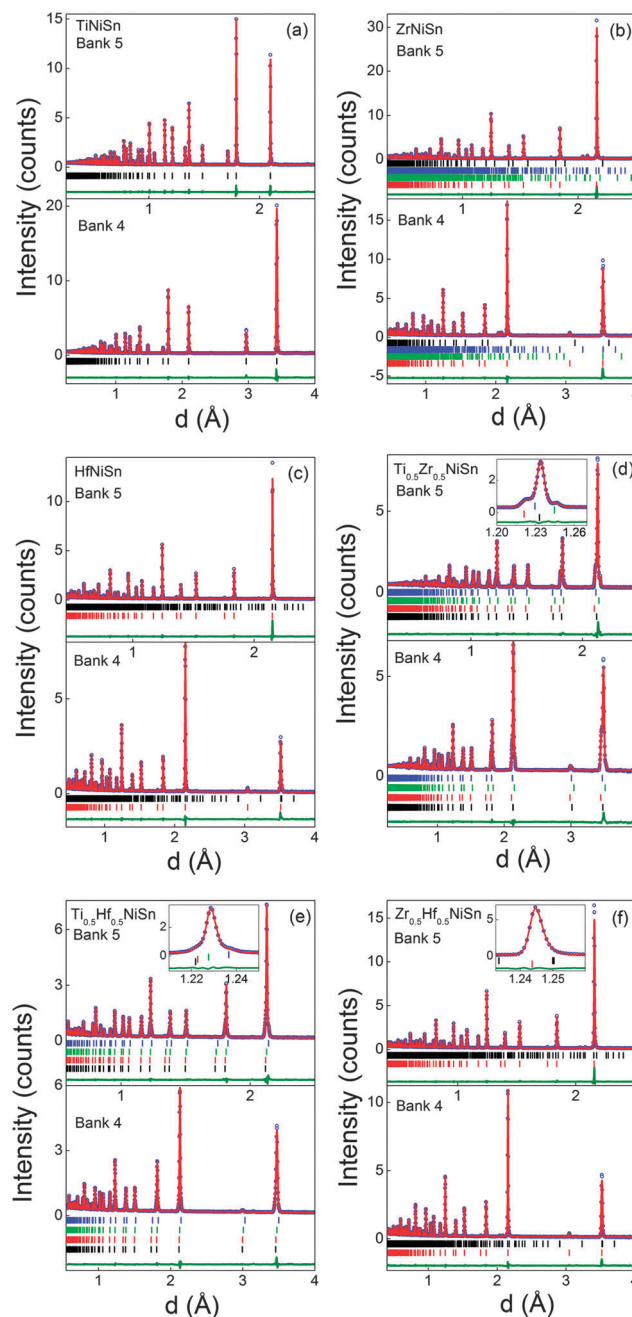

Fig. 1 Observed (circles), calculated (solid line) and difference Rietveld neutron powder diffraction profiles for (a) $TiNiSn$, (b) $ZrNiSn$, (c) $HfNiSn$, (d) $Ti_{0.5}Zr_{0.5}NiSn$, (e) $Ti_{0.5}Hf_{0.5}NiSn$ and (f) $Zr_{0.5}Hf_{0.5}NiSn$. Bragg markers correspond to the half-Heusler phases used to fit the pattern (summarised in Tables 1 and 2), except for $ZrNiSn$ where the markers are for $ZrNiSn$, Zr_5Sn_4, $Ni_{2.67}Sn_2$ and $ZrNi_2Sn$ (bottom to top). The insets in (d–f) illustrate the multiphase behaviour for samples with mixed X metals. Bank 5 and 4 are the backscattering and 90 degrees detector banks, respectively.

This journal is © The Royal Society of Chemistry 2015

J. Mater. Chem. C, 2015, **3**, 10534–10542 | **10535**

Table 1 Lattice parameter (a), fractional site occupancies (occ), thermal displacement parameters (U_{iso}/Å^2) and fit statistics for the XNiSn (X = Ti, Zr, Hf) samples

X		Ti	Zr	Hf
a (Å)		5.9298(1)	6.1089(1)	6.0795(1)
X	occ	1	1	1
	U_{iso}	0.00494(7)	0.0057(2)	0.0047(5)
Ni(1)	occ	1	1	1
	U_{iso}	0.00498(5)	0.00461(6)	0.0046(5)
Ni(2)	occ	0.024(1)	0.002(1)	0.009(2)
	U_{iso}	0.00498(5)	0.00461(6)	0.0046(5)
Sn	occ	1	1	1
	U_{iso}	0.00407(5)	0.0021(2)	0.0036(5)
wt%		100	95.00(8)	99.17(3)
χ^2		8.2	9.9	7.4
wR_p/%	Bank 5	3.4	3.0	2.8
	Bank 4	2.0	2.4	2.2
	Bank 3	2.1	2.5	2.2
R_p/%	Bank 5	4.2	4.2	5.1
	Bank 4	3.2	5.0	4.2
	Bank 3	3.6	3.0	3.0
R_f^2/%	Bank 5	5.7	7.1	8.5
	Bank 4	6.2	6.0	7.3
	Bank 3	7.5	7.2	5.3

X: 4a (0, 0, 0), Ni(1): 4c $(\frac{1}{4}, \frac{1}{4}, \frac{1}{4})$, Ni(2): 4d $(\frac{3}{4}, \frac{3}{4}, \frac{3}{4})$, Sn: 4b $(\frac{1}{2}, \frac{1}{2}, \frac{1}{2})$. ZrNiSn contains 0.93(7) wt% Zr_5Sn_4, 3.36(3) wt% $Ni_{2.67}Sn_2$ and 0.44(1) wt% $ZrNi_2Sn$. HfNiSn contains 0.83(3) wt% HfO_2. Bank 5, 4 and 3 are the backscattering, 90 degrees and low angle detector banks, respectively.

reported values.[25] Maintaining a stoichiometric TiNiSn model, with Ti, Ni and Sn on their expected sites (X, Y1, Z), results in $\chi^2 = 8.8$. Two models were subsequently identified that resulted in an improvement in χ^2. The first of these involves 2% excess Ni on the vacant tetrahedral Y2 site. The second model has 3%

inversion of Ti and Sn (*i.e.* $Ti_{0.97}Sn_{0.03}NiSn_{0.97}Ti_{0.03}$). Both models produce $\chi^2 = 8.2$ ($\chi^2 = 7.9$ from a LeBail fit). Larger degrees of inversion are needed for the previously reported $TiNi_{1.04}Sn$ (6% inversion) and $TiNi_{1.06}Sn$ (10% inversion) samples.[7] A nominal $TiNiSn_{0.95}$ sample was also prepared by standard solid state reaction and best-fit models were found for $TiNi_{1.056(2)}Sn$ or 9% Ti–Sn inversion. Furthermore, HfNiSn requires 30% inversion of Hf and Sn, or <1% excess Ni. ZrNiSn was found to be stoichiometric despite the presence of Zr_5Sn_4 and $Ni_{2.67}Sn_2$ secondary phases. The much smaller variation in Y2 site occupancies suggests that the presence of excess Ni is the most plausible interpretation of our data. This is in keeping with the covalent bonding in these structures and the large energetic cost for X/Sn inversion.[39]

$Ti_{0.5}Zr_{0.5}NiSn$. Our previous work demonstrated that the ingots with mixed X metals are not phase pure but contain multiple $X_{1-x}X'_xNiSn$ half-Heusler phases.[25] A total of 4 half-Heusler phases were used to fit the NPD data, as shown in the inset to Fig. 1d. The lattice and atomic parameters for the 4 phases are presented in Table 2. The Zr content of each phase was calculated from the lattice parameters using Vegard's law (x_V) and by refining the X-site occupancy (x_R). It was not possible to determine x_R for the most minor phase, present at 3 wt%, and the occupancies were kept fixed at the x_V values. The x_R values are plotted against x_V in Fig. 2a. From this figure, it may be seen that, for $x_V \geq 0.5$, there is good agreement between x_R and x_V. At lower values of x_V however, the refined x_V are somewhat larger than x_R. This indicates a departure from Vegard's law with the x_R indicating a lower Zr-fraction than that derived from the lattice parameter. This discrepancy does not lead to any significant difference in average composition of the multiphase samples. The highest resolution backscattering

Table 2 Lattice parameters (a), weight percentages (wt%), fractional site occupancies (occ), thermal displacement parameters (U_{iso}/Å^2), x_V calculated from Vegard's law, x_R obtained from the refined X-site occupancies, compositional spread (Δx), and fit statistics for the $X_{1-x}X'_xNiSn$ phases present in the $X_{0.5}X'_{0.5}NiSn$ samples (X, X' = Ti, Zr, Hf)

a (Å)	wt%		X/X'	Ni(1)	Ni(2)	Sn	x_V	x_R	Δx	χ^2	Bank	wR_p	R_p	R_f^2
$Ti_{0.5}Zr_{0.5}NiSn$/fitted composition: $Ti_{0.495(7)}Zr_{0.505(7)}Ni_{1.028(3)}Sn$														
5.9815(2)	18.3(2)	occ	0.847(3)/0.153(3)	1	0.052(2)	1	0.29(1)	0.153(3)	0.12(1)	5.5				
		U_{iso}	0.0052(1)	0.0052(1)	0.0052(1)	0.0052(1)								
6.0240(2)	19.7(7)	occ	0.53(1)/0.47(1)	1	−0.003(8)	1	0.5(1)	0.47(1)	0.10(1)		5	2.8	4.6	5.9
		U_{iso}	0.00213(4)	0.00213(4)	0.00213(4)	0.00213(4)					4	1.6	2.9	3.6
6.0406(1)	59.2(7)	occ	0.412(6)/0.588(6)	1	0.032(4)	1	0.62(1)	0.588(6)	0.07(1)		3	1.7	2.9	5.4
		U_{iso}	0.00653(4)	0.00653(4)	0.00653(4)	0.00653(4)								
6.1020(2)	2.7(1)	occ	0.04/0.96	1	0	1	0.96(1)	0.96	0.06(1)					
		U_{iso}	0.0010(2)	0.0010(2)	0.0010(2)	0.0010(2)								
$Ti_{0.5}Hf_{0.5}NiSn$/fitted composition: $Ti_{0.53(1)}Hf_{0.47(1)}Ni_{1.019(5)}Sn$														
5.9834(3)	14(1)	occ	0.805(5)/0.195(5)	1	0.030(4)	1	0.36(1)	0.195(5)	0.12(1)	6.0				
		U_{iso}	0.0050(2)	0.0050(2)	0.0050(2)	0.0054(2)								
6.0046(3)	23(1)	occ	0.46(2)/0.54(2)	1	0.00(2)	1	0.50(1)	0.54(2)	0.04(1)		5	2.0	2.7	1.8
		U_{iso}	0.00524(5)	0.00524(5)	0.00524(5)	0.00524(5)					4	1.5	2.6	4.8
6.0157(1)	60.1(9)	occ	0.419(9)/0.581(9)	1	0.024(6)	1	0.57(1)	0.581(9)	0.03(1)		3	2.0	2.5	2.8
		U_{iso}	0.00524(5)	0.00524(5)	0.00524(5)	0.00524(5)								
6.0604(3)	3.0(8)	occ	0.13/0.87	1	0	1	0.87(1)	0.87	0.08(1)					
		U_{iso}	0.00007(7)	0.00007(7)	0.00007(7)	0.00007(7)								
$Zr_{0.5}Hf_{0.5}NiSn$/fitted composition: $Zr_{0.59(4)}Hf_{0.41(4)}Ni_{1.002(3)}Sn$														
6.0926(1)	98.9(1)	occ	0.59(4)/0.41(4)	1	0.002(3)	1	0.49(1)	0.59(4)	0.14(1)	10.9	5	2.1	4.4	6.0
		U_{iso}	0.0066(2)	0.00495(6)	0.00495(6)	0.0017(2)					4	2.0	3.1	5.1
											3	2.9	3.7	3.2

$Zr_{0.5}Hf_{0.5}NiSn$ contains 1.1(1) wt% $Ni_{2.67}Sn_2$.

10536 | J. Mater. Chem. C, 2015, 3, 10534–10542
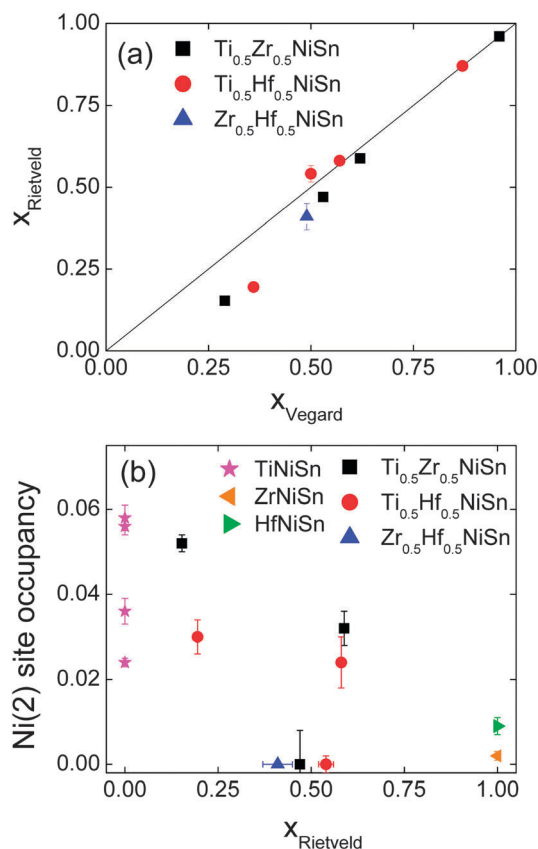
This journal is © The Royal Society of Chemistry 2015

Fig. 2 (a) Fitted X-metal fractions (x_R) against those calculated from Vegard's law (x_V) (b) Ni(2) site occupancy for the $X_{1-x}X'_xNi_{1+y}Sn$ phases present in the $X_{0.5}X'_{0.5}NiSn$ samples (X, X' = Ti, Zr, Hf). Additional TiNiSn data from ref. 7.

detector (bank 5) was used to get an estimate of any peak broadening caused by further compositional fluctuations (Δx).[25] All profile function parameters, except γ_1 which models microstrain, were kept fixed at the average value for the XNiSn end-members. For a cubic system, the microstrain can be easily related to a spread in x value,[25] and the calculated values for Δx are tabulated in Table 2 and are shown in Fig. 3a. Refinement of the Y2 site occupancy revealed that Ni partially occupies the Y2 site in 2 of the 4 HH phases (Table 2). The largest excess of Ni ($y = 0.052(2)$) was found in the phase with $x_R = 0.153(3)$. The average composition of this sample was found to be $Ti_{0.495(7)}Zr_{0.505(7)}Ni_{1.028(3)}Sn$, which is in good agreement with the nominal x value and indicates the presence of 3% excess Ni.

$Ti_{0.5}Hf_{0.5}NiSn$. This sample shows similar multiphase behaviour to $Ti_{0.5}Zr_{0.5}NiSn$ and was analysed analogously. The refined Hf occupancies were found to be x_R = 0.195(5), 0.54(2), 0.581(9) and 0.87, where the last value was fixed to x_V due to the low abundance of this phase. The x_R values are in good agreement with x_V for $x_V \geq 0.5$, with a small discrepancy for lower x, as seen for $Ti_{0.5}Zr_{0.5}NiSn$ (Fig. 2a). The Δx values are comparable to those found in $Ti_{0.5}Zr_{0.5}NiSn$ and are shown in Fig. 3b. Two of the HH phases were found to contain Ni on the Y2 site. The refined values are presented in Table 2 and the Ni content is plotted in Fig. 2b. The average composition was found to be $Ti_{0.53(1)}Hf_{0.47(1)}Ni_{1.019(5)}Sn$.
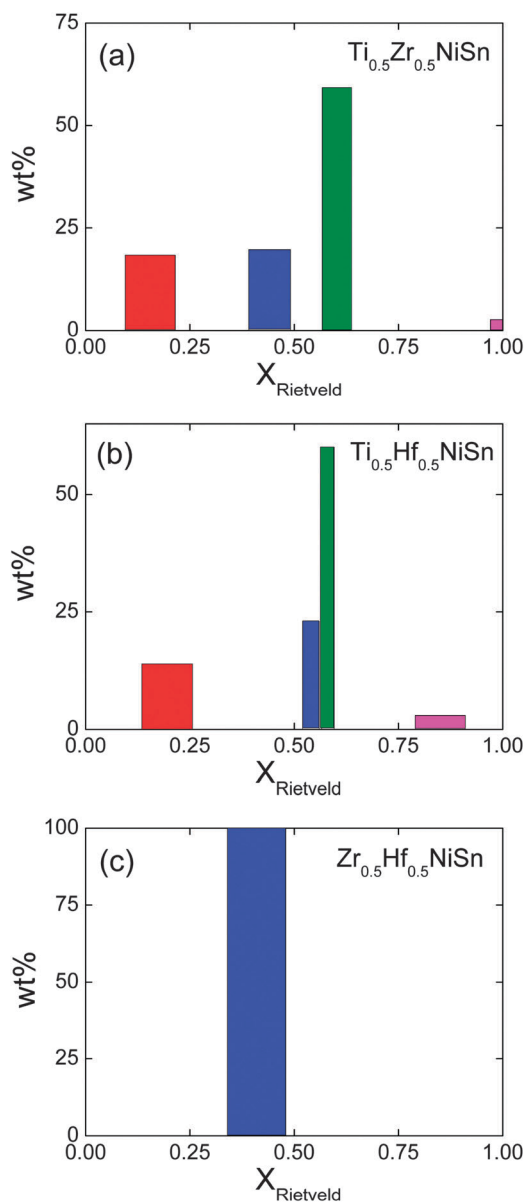

Fig. 3 Histograms of the phase distribution and compositional spread of the $X_{1-x}X'_xNiSn$ phases present in the $X_{0.5}X'_{0.5}NiSn$ samples (X = Ti, Zr, Hf). The centre and widths of the bars correspond to x_R and Δx.

$Zr_{0.5}Hf_{0.5}NiSn$. The narrow range of unit cell parameters observed for this composition (due to the similar radii of Zr and Hf) means only one phase could be identified, instead of the three that were observable in the X-ray data (Fig. 1f).[25] The lattice and atomic parameters are presented in Table 2. Refinement of the Y2 site occupancy suggested this sample is stoichiometric, and does not contain any excess Ni. The final fitted composition of this sample was found to be $Zr_{0.59(4)}Hf_{0.41(4)}Ni_{1.002(3)}Sn$, consistent with the X-ray data,[25] and the nominal composition.

2. Temperature dependence studies

TiNiSn. The fitted lattice parameters, fractional site occupancies and fit statistics are presented in Table 3. The unit cell volume was found to increase linearly above 300 K, as illustrated in Fig. 4a.

This journal is © The Royal Society of Chemistry 2015

J. Mater. Chem. C, 2015, **3**, 10534–10542 | **10537**

The volume expansion could be fitted by $V(T) = V_0 + A \coth(\theta_D/T)$, where A is a scale factor and θ_D is the Debye temperature. From this fit $V_0 = 205.4(1)$ Å^3, $A = 2.6(2)$ and $\theta_D = 347(22)$ K. This is consistent with literature values which put θ_D in the range 360–420 K.[43] The temperature dependence of the thermal displacement parameters (U_{iso}) of each atom are plotted in Fig. 4b. The similar gradients and magnitudes indicate that all three atom types vibrate at around the same frequency. The values for Sn are slightly reduced compared with Ti and Ni due to its larger mass. Using the average slope and mass of TiNiSn a Debye temperature of 367(2) K was obtained,[44] in excellent agreement with the value from the fit to cell volume, and the literature. The Ni occupancies on the Y1 and Y2 sites were also refined for each temperature step and remained constant within one estimated standard deviation (Table 3).

Ti$_{0.5}$Hf$_{0.5}$NiSn. The fitted lattice parameters, weight fractions, site occupancies and fit statistics are presented in Table 4. The lattice parameters for each phase were found to increase linearly with temperature. The increase in temperature was found to have very little effect on the distribution of the phases in this sample. The Ti : Hf ratio remained almost constant for each phase, while Ni(2) site occupancy was found to decrease somewhat at the highest measured temperatures. The weight fractions of each of the phases remained constant between 273 and 873 K. The overall composition and distribution of phases therefore do not change significantly with temperature. The temperature dependence of the average thermal displacement parameters for the two most abundant phases was used to estimate the Debye temperature, which was calculated to be 317(2) K.

3. Thermoelectric properties

The use of band models to fit experimental thermoelectric data is increasingly common. The simplest of these models is the single parabolic band model which is most readily applied in the high temperature and degenerate semiconducting limit,[45]
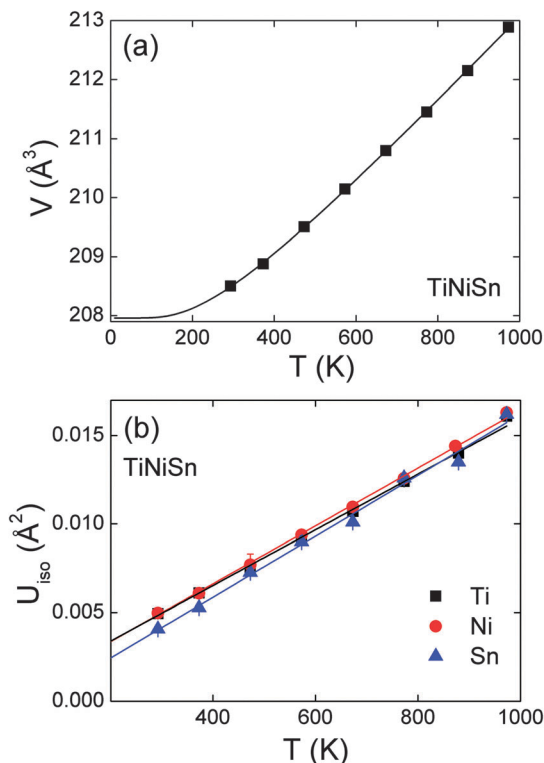

Fig. 4 (a) Temperature dependence of the unit cell volume for TiNiSn. The solid line is a fit (see manuscript text). (b) Temperature dependence of the thermal displacement parameters of Ti, Ni and Sn.

where the chemical carrier concentration (n) is assumed constant. The $\rho(T)$ of electron doped Ti$_{0.5}$Zr$_{0.5}$NiSn$_{1-z}$Sb$_z$ samples ($z = 0.005$, 0.01 and 0.02) is shown on a log–log plot in Fig. 5a. The slopes fall between 0.2–0.7, where values between 1–1.5 are expected for electron transport limited by acoustic phonon scattering. The lower values observed here are characteristic of alloy scattering.[45] As both acoustic and alloy scattering are energy independent, an

Table 3 Temperature evolution of the lattice parameter (a), thermal displacement parameters (U_{iso}/Å^2), Y2 site occupancy (occ) and fit statistics for TiNiSn between 293 and 973 K

		293 K	373 K	473 K	573 K	673 K	773 K	873 K	973 K
a (Å)		5.9297(1)	5.9333(1)	5.9329(1)	5.9453(1)	5.9514(1)	5.9576(1)	5.9641(1)	5.9710(1)
Ti	U_{iso}	0.00495(7)	0.0061(1)	0.0078(1)	0.0095(2)	0.0107(2)	0.0130(2)	0.0142(3)	0.0167(2)
Ni(1)	U_{iso}	0.00499(5)	0.00609(6)	0.0078(1)	0.00946(7)	0.01099(9)	0.01276(9)	0.0147(2)	0.0164(1)
Ni(2)	occ	0.022(1)	0.019(1)	0.019(1)	0.018(1)	0.019(1)	0.015(1)	0.020(1)	0.015(1)
	U_{iso}	0.00499(5)	0.00609(6)	0.0078(1)	0.00946(7)	0.01099(9)	0.01276(9)	0.0147(2)	0.0164(1)
Sn	U_{iso}	0.0045(6)	0.00527(9)	0.00703(1)	0.0066(9)	0.0099(1)	0.0119(2)	0.0134(2)	0.0155(1)
χ^2		8.6	4.1	4.0	4.0	3.8	4.1	4.1	4.3
wR_p	Bank 5	3.1	2.0	2.0	2.1	2.1	2.2	2.2	2.3
	Bank 4	2.0	1.4	1.3	1.3	1.2	1.2	1.2	1.4
	Bank 3	2.1	1.0	1.2	1.1	1.1	1.3	1.2	1.3
R_p	Bank 5	3.6	2.3	2.5	2.4	2.5	2.6	2.7	2.7
	Bank 4	3.2	2.8	2.3	2.3	2.3	2.1	2.0	2.2
	Bank 3	3.6	1.1	1.3	1.2	1.1	1.4	1.3	1.4
R_f^2	Bank 5	5.4	3.4	3.6	4.1	4.5	5.7	6.4	6.4
	Bank 4	6.2	4.3	4.7	7.8	7.5	8.3	8.9	10.7
	Bank 3	7.6	7.5	7.5	10.9	10.5	11.5	10.8	10.0

The 293 K pattern was collected outside of the furnace.

10538 | *J. Mater. Chem. C*, 2015, **3**, 10534–10542

This journal is © The Royal Society of Chemistry 2015

Table 4 Temperature evolution of the lattice parameters (a), fitted Hf fractions (x), Ni(2) site occupancy, weight percentages (wt%), thermal displacement parameters (U_{iso}/Å^2) and fit statistics for the Ti$_{1-x}$Hf$_x$NiSn phases present in the Ti$_{0.5}$Hf$_{0.5}$NiSn sample

Phase		293 K	473 K	673 K	873 K
1	a (Å)	5.9834(3)	5.9950(3)	6.0074(6)	6.0192(5)
	x	0.195(5)	0.223(5)	0.210(9)	0.206(8)
	Ni(2)	0.030(4)	0.027(4)	0.016(5)	0.011(7)
	Wt%	14(1)	16(1)	16(1)	15.5(2)
	U_{iso}	0.0050(2)	0.0060(2)	0.0088(2)	0.0132(4)
2	a (Å)	6.0046(3)	6.0164(2)	6.0285(3)	6.0394(4)
	x	0.54(3)	0.559(9)	0.57(1)	0.59(2)
	Ni(2)	0.00(2)	0	0	0
	Wt%	23(1)	27.6(7)	29.8(9)	25.2(1)
	U_{iso}	0.00524(5)	0.00770(4)	0.01068(5)	0.01378(8)
3	a (Å)	6.0157(1)	6.0262(1)	6.0378(1)	6.0490(1)
	x	0.581(9)	0.588(9)	0.610(5)	0.592(6)
	Ni(2)	0.024(6)	0.022(5)	0	0
	Wt%	60.1(9)	54.0(7)	51.8(9)	56.3(1)
	U_{iso}	0.00524(5)	0.00770(4)	0.01068(5)	0.01378(8)
4	a (Å)	6.0604(3)	6.0691(4)	6.0800(4)	6.0919(7)
	x	0.87	0.87	0.87	0.87
	Ni(2)	0	0	0	0
	Wt%	3.0(8)	2.8(1)	2.9(1)	2.9(2)
	U_{iso}	0.0001(3)	0.0004(5)	0.0021(6)	0.0050(9)
Current[a]		450	200	200	75
χ^2		6.0	2.4	2.4	1.0
wR_p	Bank 5	2.0	1.4	1.4	1.7
	Bank 4	1.5	1.0	1.3	1.4
	Bank 3	2.0	2.2	1.9	1.5
R_p	Bank 5	2.7	2.5	2.4	2.9
	Bank 4	2.6	1.6	2.8	3.3
	Bank 3	2.5	2.5	2.2	2.0
R_f^2	Bank 5	1.8	3.0	3.6	5.2
	Bank 4	4.8	8.8	9.8	7.0
	Bank 3	2.8	3.5	5.3	9.4

[a] Integrated proton beam current to ISIS target/μA h.

identical $S(T)$ is expected,[46] and the familiar expressions for S and n can be used:

$$S = \frac{k}{e}\left(\frac{2F_1}{F_0} - \eta\right) \qquad (1)$$

$$n = 4\pi\left(\frac{2m^*kT}{h^2}\right)^{3/2} F_{1/2} \qquad (2)$$

Here, k is Boltzmann's constant, e the electron charge, h is Planck's constant, m^* is the effective carrier mass, η is the reduced Fermi level measured from the conduction band minimum (E_F/kT), and F_j are the Fermi integrals, which were evaluated numerically (ε is the reduced energy):

$$F_j(\eta) = \int_0^\infty \frac{\varepsilon^j d\varepsilon}{1 + \mathrm{Exp}[\varepsilon - \eta]} \qquad (3)$$

The magnitude of S is therefore only a function of η (eqn (1)), while m^* can be evaluated using the η value gained from the experimental S, and the chemical carrier concentration (eqn (2)). The calculated carrier concentrations were ($z = 0.005$, 9.15×10^{25} m^{-3}), ($z = 0.01$, 1.83×10^{26} m^{-3}) and ($z = 0.02$, 3.66×10^{26} m^{-3}) and the obtained

m^* values are 2.33 m_e ($z = 0.005$), 2.51 m_e ($z = 0.01$) and 2.64 m_e ($z = 0.02$) where m_e is the electron mass. These values are in good agreement with published data for ZrNi$_{1+y}$Sn HH alloys.[47,48] As a further test of the validity of the SPB model we calculated the predicted temperature dependence of S using the constant carrier approximation, and these curves are plotted in Fig. 5b. There is a good agreement below 400 K, while S is overestimated above this temperature, which typically signals the presence of minority charge carriers. The $\rho(T)$ and $S(T)$ for the non-Sb doped (non-degenerate) samples containing Ti are shown in Fig. 5c and d. The $\rho(T)$ follows a thermally activated temperature dependence over the entire measured temperature interval (300–730 K). The fitted bandgap values are $E_g = 0.12$–0.15 eV (see Table 5) which is much smaller than the 0.45 eV gap predicted from first principles calculations.[49] The observation of reduced bandgaps is common for HHs,[50] and points towards the presence of in-gap states due to structural disorder and/or excess Ni.[36] Similar bandgap values are observed for SPS processed Ti$_{0.5}$Zr$_{0.5}$NiSn samples,[51] demonstrating that these values are not affected strongly by porosity. The $S(T)$ for these compositions shows a gradual monotonous decrease (Fig. 5d). By contrast, the $S(T)$ for samples containing Zr and Hf are characterised by a maximum near 350 K (X = Zr) and 550 K (X = Zr$_{0.5}$Hf$_{0.5}$, Hf), followed by a rapid decrease (Fig. 5f). This rapid decrease is caused by the onset of minority carrier (p-type) conduction, which is also evident in the $\rho(T)$ data (Fig. 5e). The maximum for X = Zr is lower than reported in the literature (550 K),[52] and this may be linked to presence of impurity phases in this sample (Table 1). The $\ln \rho(T) - 1/T$ data for the samples without Ti are shown in Fig. 5e, and reveals the presence of similar bandgap values below the onset of minority carrier conduction (0.07–0.16 eV, Table 5). In addition, the Goldsmid–Sharp formula was used to extract a value for the bandgap from the $S(T)$ data.[53] These are larger and fall between 0.3–0.4 eV (Table 5). The discrepancy between the bandgap values from $\rho(T)$ and $S(T)$ data has recently been discussed and results from the mobility difference between electrons and holes, and leads to overestimates when using the classical Goldsmid–Sharp equation.[50] The bandgap values observed here are consistent with recently reported values of 0.13 eV for ZrNiSn from room temperature optical measurements.[50]

Discussion

There is now substantial evidence confirming that there is no solubility of excess Ni in the HH structure, and that segregation into a HH matrix and FH inclusions occurs.[3,6] We have previously reported extensive electron microscopy characterisation of a TiNi$_{1.05}$Sn sample which was prepared in an identical manner to the samples discussed here (e.g. by solid state reactions without post synthesis processing).[18] This revealed that the excess Ni is finely dispersed within the matrix with a limit <2 nm on the size of the nanoinclusions. We also demonstrated that ~2% additional Ni was present in all TiNiM$_y$Sn samples investigated. This was attributed to the stability of competing Ti–Sn binary phases. The observation
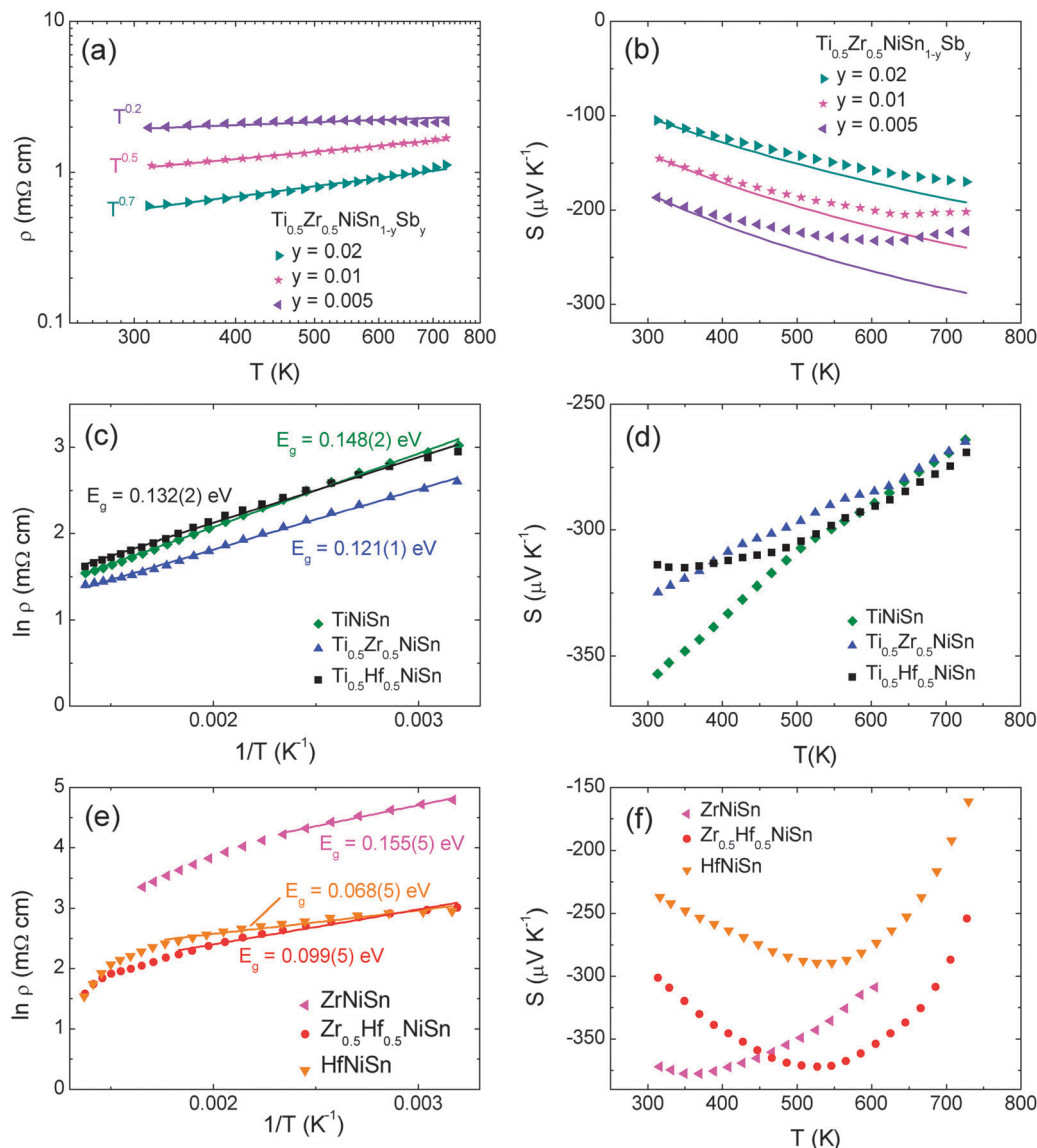
This journal is © The Royal Society of Chemistry 2015

J. Mater. Chem. C, 2015, **3**, 10534–10542 | **10539**

Fig. 5 Temperature dependence of the electrical resistivity and Seebeck coefficient for (a and b) degenerately doped $Ti_{0.5}Zr_{0.5}NiSn_{1−z}Sb_z$ (c and d) non-degenerate XNiSn samples containing X = Ti and (e and f) non-degenerate XNiSn samples with X = Zr, Hf.

Table 5 Summary of bandgap values and pre-exponential factors obtained from fits to electrical resistivity data, and thermal bandgap values obtained using the Goldsmid−Sharp formula[53]

Composition	Fitting range (K)	E_g (eV)	ρ_0 (mΩ cm)	$E_g = 2e|S_{max}|T_{max}$
TiNiSn	300–730	0.148(2)	1.43(8)	
$Ti_{0.5}Zr_{0.5}NiSn$	300–730	0.121(1)	1.51(8)	
$Ti_{0.5}Hf_{0.5}NiSn$	300–730	0.132(2)	1.80(9)	
ZrNiSn	300–450	0.155(5)	13.7(2)	0.271(8)
$Zr_{0.5}Hf_{0.5}NiSn$	300–570	0.099(5)	3.5(2)	0.392(7)
HfNiSn	300–570	0.068(5)	6.0(2)	0.310(5)

of 2–3% excess Ni for the samples containing Ti, and the absence of excess Ni for samples with X = Zr, Hf (Tables 1 and 2), is in keeping with this earlier observation and emphasises the need for a tight control of the synthesis conditions. One of the most

striking features of the transport data is the gradual decrease of $S(T)$ for samples containing Ti, and the absence of an ambipolar transition (the onset of minority carrier conduction). This occurs for both TiNiSn and the multiphase samples, suggesting that the phase segregation has limited impact. Density functional theory calculations reveal similar bandstructures for X = Ti, Zr and Hf with an indirect gap of ∼0.45 eV between the Γ and X points,[49] and it is therefore not immediately apparent why $S(T)$ behaves differently. As the experimental bandgaps are also rather similar, it is tempting to link the absence of minority carrier conduction to the presence of electron doping from the 2–3% excess Ni in these samples. However, literature data reveals that the ambipolar transition survives in $ZrNi_{1+y}Sn$ samples with 6% excess Ni,[47,52] suggesting that there may not be a link to the amount of excess Ni, or that it may depend on the exact nature of the phase segregation. The $ZrNi_{1+y}Sn$ samples were prepared from the melt

10540 | J. Mater. Chem. C, 2015, 3, 10534–10542

This journal is © The Royal Society of Chemistry 2015

and it is likely that this will cause a difference in the degree of segregation of the FH phases. This can have a significant impact on the properties: for example the changes in $S(T)$ and $\rho(T)$ in the TiNi$_{1+y}$Sn series with finely dispersed excess Ni are consistent with conventional doping,[18] whereas enhancements in S due to carrier filtering were observed in hot-pressed compositions containing well-defined FH inclusions.[14] Further work is needed to fully elucidate the difference in behaviour between the samples that contain Ti and those that do not. Another plausible explanation is that the difference in behaviour is linked to a microstructural effect that only occurs in the presence of Ti, and is not directly linked to either the multiphase behaviour or the presence of excess Ni. The $S(T)$ for degenerately doped Ti$_{0.5}$Zr$_{0.5}$NiSn$_{1-z}$Sb$_z$ samples can be modelled adequately using a single parabolic band model with the mobility limited by alloy scattering. The observation of carrier transport limited by alloy scattering is reasonable as the compositional changes due to phase segregation of the X-site metals occur over relatively large lengthscales (>5 μm).[20,21,25] These distances are greater than typical electron mean free paths, and are therefore not expected to impact strongly on the carrier transport.

Neutrons probe a larger sample volume than X-rays, and the phase distributions in the multiphase samples (Fig. 3) are significantly narrower than determined from X-ray data. The present data are more representative of the bulk, suggesting that 3–4 discrete phases are indeed present with the broadening of the individual HH X-ray and neutron profiles (quantified as Δx) at least partially due to microstrain effects and not solely linked to compositional variations. Some of the refined compositions fall outside of the thermodynamic limits for mixing of the X-metals,[6] suggesting that the final observed phase distribution is kinetically controlled. The temperature-dependent neutron diffraction study into TiNiSn and Ti$_{0.5}$Hf$_{0.5}$NiSn showed no significant change in phase-distribution as the temperature was increased (Fig. 4, Tables 3 and 4). In addition to the temperature steps reported in Table 4, this sample was held at 600 °C for 6 hours and re-measured at regular intervals. The reflections remained the same shape throughout, indicating no change in the distribution. In terms of application this highlights that these materials show stability to prolonged exposure to high temperatures, which is of vital importance for thermoelectric materials. The variable temperature data also afforded the extraction of a reliable estimate of the Debye temperatures for TiNiSn ($\theta_D = 367(2)$ K) and Ti$_{0.5}$Hf$_{0.5}$NiSn ($\theta_D = 317(2)$ K).

The main conclusion is that XNiSn half-Heuslers samples are susceptible to phase segregation as exemplified by the presence of distinct half-Heusler compositions for samples with mixtures of X metals, and full-Heusler domains in samples containing Ti. The onset of minority carrier conduction observed for XNiSn samples with Zr and Hf is suppressed in the samples containing Ti.

Acknowledgements

References

1 *Thermoelectrics and its Energy Harvesting*, ed. D. M. Rowe, CRC Press, Boca Raton, 2012.

2 H. Hohl, A. P. Ramirez, W. Kaefer, K. Fess, C. Thurner, C. Kloc and E. Bucher, *Thermoelectric Materials – New Directions and Approaches*, 1997, pp. 109–114.

3 J. W. G. Bos and R. A. Downie, *J. Phys.: Condens. Matter*, 2014, **26**, 433201.

4 S. Chen and Z. F. Ren, *Mater. Today*, 2013, **16**, 387–395.

5 W. J. Xie, A. Weidenkaff, X. F. Tang, Q. J. Zhang, J. Poon and T. M. Tritt, *Nanomaterials*, 2012, **2**, 379–412.

6 Y. Kimura and Y. W. Chai, *JOM*, 2015, **67**, 233–245.

7 R. A. Downie, D. A. MacLaren, R. I. Smith and J. W. G. Bos, *Chem. Commun.*, 2013, **49**, 4184–4186.

8 Y. W. Chai and Y. Kimura, *Appl. Phys. Lett.*, 2012, **100**, 033114.

9 Y. W. Chai and Y. Kimura, *Acta Mater.*, 2013, **61**, 6684–6697.

10 H. Hazama, M. Matsubara, R. Asahi and T. Takeuchi, *J. Appl. Phys.*, 2011, **110**, 063710.

11 C. S. Birkel, J. E. Douglas, B. R. Lettiere, G. Seward, N. Verma, Y. Zhang, T. M. Pollock, R. Seshadri and G. D. Stucky, *Phys. Chem. Chem. Phys.*, 2013, **15**, 6990–6997.

12 J. E. Douglas, C. S. Birkel, M.-S. Miao, C. J. Torbet, G. D. Stucky, T. M. Pollock and R. Seshadri, *Appl. Phys. Lett.*, 2012, **101**, 183902.

13 H. Hazama, R. Asahi, M. Matsubara and T. Takeuchi, *J. Electron. Mater.*, 2010, **39**, 1549–1553.

14 J. P. A. Makongo, D. K. Misra, X. Zhou, A. Pant, M. R. Shabetai, X. Su, C. Uher, K. L. Stokes and P. F. P. Poudeu, *J. Am. Chem. Soc.*, 2011, **133**, 18843–18852.

15 P. Sahoo, Y. Liu, J. P. A. Makongo, X.-L. Su, S. J. Kim, N. Takas, H. Chi, C. Uher, X. Pan and P. F. P. Poudeu, *Nanoscale*, 2013, **5**, 9419–9427.

16 Y. Liu, P. Sahoo, J. P. A. Makongo, X. Zhou, S.-J. Kim, H. Chi, C. Uher, X. Pan and P. F. P. Poudeu, *J. Am. Chem. Soc.*, 2013, **135**, 7486–7495.

17 S. V. Faleev and F. Léonard, *Phys. Rev. B: Condens. Matter Mater. Phys.*, 2008, **77**, 214304.

18 R. A. Downie, R. I. Smith, D. A. MacLaren and J. W. G. Bos, *Chem. Mater.*, 2015, **27**, 2449–2459.

19 S. Sakurada and N. Shutoh, *Appl. Phys. Lett.*, 2005, **86**, 082105.

20 S. Populoh, M. H. Aguirre, O. C. Brunko, K. Galazka, Y. Lu and A. Weidenkaff, *Scr. Mater.*, 2012, **66**, 1073–1076.

21 M. Schwall and B. Balke, *Phys. Chem. Chem. Phys.*, 2013, **15**, 1868–1872.

22 E. Rausch, B. Balke, T. Deschauer, S. Ouardi and C. Felser, *APL Mater.*, 2015, **3**, 041516.

23 E. Rausch, B. Balke, S. Ouardi and C. Felser, *Phys. Chem. Chem. Phys.*, 2014, **16**, 25258–25262.

24 H. Y. Geng and H. Zhang, *J. Appl. Phys.*, 2014, **116**, 033708.

25 R. A. Downie, D. A. MacLaren and J. W. G. Bos, *J. Mater. Chem. A*, 2014, **2**, 6107–6114.

26 D. K. Misra, A. Bhardwaj and S. Singh, *J. Mater. Chem. A*, 2014, **2**, 11913–11921.

27 D. K. Misra, A. Rajput, A. Bhardwaj, N. S. Chauhan and S. Singh, *Appl. Phys. Lett.*, 2015, **106**, 103901.

28 A. Bhardwaj and D. K. Misra, *J. Mater. Chem. A*, 2014, **2**, 20980–20989.

29 W. J. Xie, Y. G. Yan, S. Zhu, M. Zhou, S. Populoh, K. Galazka, S. J. Poon, A. Weidenkaff, J. He, X. F. Tang and T. M. Tritt, *Acta Mater.*, 2013, **61**, 2087–2094.

30 W. J. Xie, J. He, S. Zhu, X. L. Su, S. Y. Wang, T. Holgate, J. W. Graff, V. Ponnambalam, S. J. Poon, X. F. Tang, Q. J. Zhang and T. M. Tritt, *Acta Mater.*, 2010, **58**, 4705–4713.

31 T. Graf, P. Klaer, J. Barth, B. Balke, H. J. Elmers and C. Felser, *Scr. Mater.*, 2010, **63**, 1216–1219.

32 J. E. Douglas, P. A. Chater, C. M. Brown, T. M. Pollock and R. Seshadri, *J. Appl. Phys.*, 2014, **116**, 163514.

33 A. C. Larson and R. B. Von Dreele, *Los Alamos National Laboratory Report LAUR*, 2000, pp. 86–748.

34 B. H. Toby, *J. Appl. Crystallogr.*, 2001, **34**, 210–213.

35 T. Graf, C. Felser and S. S. P. Parkin, *Prog. Solid State Chem.*, 2011, **39**, 1–50.

36 D. T. Do, S. D. Mahanti and J. J. Pulikkoti, *J. Phys.: Condens. Matter*, 2014, **26**, 275501.

37 K. Kirievsky, Y. Gelbstein and D. Fuks, *J. Solid State Chem.*, 2013, **203**, 247–254.

38 K. Kirievsky, M. Shlimovich, D. Fuks and Y. Gelbstein, *Phys. Chem. Chem. Phys.*, 2014, **16**, 20023–20029.

39 P. Larson, S. D. Mahanti and M. G. Kanatzidis, *Phys. Rev. B: Condens. Matter Mater. Phys.*, 2000, **62**, 12754–12762.

40 V. V. Romaka, P. Rogl, L. Romaka, Y. Stadnyk, N. Melnychenko, A. Grytsiv, M. Falmbigl and N. Skryabina, *J. Solid State Chem.*, 2013, **197**, 103–112.

41 Y. V. Stadnyk and R. V. Skolozdra, *Inorg. Mater.*, 1991, **27**, 1884–1885.

42 J. E. Douglas, C. S. Birkel, N. Verma, V. M. Miller, M.-S. Miao, G. D. Stucky, T. M. Pollock and R. Seshadri, *J. Appl. Phys.*, 2014, **115**, 043720.

43 P. Hermet, K. Niedziolka and P. Jund, *RSC Adv.*, 2013, **3**, 22176–22184.

44 B. C. Sales, D. G. Mandrus and B. C. Chakoumakos, in *Recent Trends in Thermoelectrics Materials Research II*, ed. T. M. Tritt, Academic Press, San Diego, 2001, pp. 1–34.

45 A. F. May and G. J. Snyder, in *Thermoelectrics and its Energy Harvesting*, ed. D. M. Rowe, CRC press, Boca Raton, 2012.

46 W. Liu, H. Chi, H. Sun, Q. Zhang, K. Yin, X. Tang, Q. Zhang and C. Uher, *Phys. Chem. Chem. Phys.*, 2014, **16**, 6893–6897.

47 H. H. Xie, H. Wang, C. G. Fu, Y. T. Liu, G. J. Snyder, X. B. Zhao and T. J. Zhu, *Sci. Rep.*, 2014, **4**, 6888.

48 H. H. Xie, H. Wang, Y. Z. Pei, C. G. Fu, X. H. Liu, G. J. Snyder, X. B. Zhao and T. J. Zhu, *Adv. Funct. Mater.*, 2013, **23**, 5123–5130.

49 S. Ogut and K. Rabe, *Phys. Rev. B: Condens. Matter Mater. Phys.*, 1995, **51**, 10443.

50 J. Schmitt, Z. M. Gibbs, G. J. Snyder and C. Felser, *Mater. Horiz.*, 2015, **2**, 68–75.

51 R. A. Downie, S. R. Popuri, H. P. Ning, M. J. Reece and J. W. G. Bos, *Materials*, 2014, **7**, 7093–7104.

52 H.-H. Xie, J.-L. Mi, L.-P. Hu, N. Lock, M. Chirstensen, C.-G. Fu, B. B. Iversen, X.-B. Zhao and T.-J. Zhu, *CrystEngComm*, 2012, **14**, 4467–4471.

53 H. J. Goldsmid and J. W. Sharp, *J. Electron. Mater.*, 1999, **28**, 869–872.

10542 | *J. Mater. Chem. C*, 2015, **3**, 10534–10542

This journal is © The Royal Society of Chemistry 2015